Three-Dimensional Flow Simulations in the Recessed Region of a Coaxial Injector

Byoung-Do Kim,[*] Stephen D. Heister,[†] and Steven H. Collicott[‡]
Purdue University, West Lafayette, Indiana 47097

A three-dimensional, two-phase, unsteady Navier–Stokes solver has been developed to investigate fluid dynamic instabilities within the recessed region of a shear coaxial injector element. Here, the main emphasis is to study applications related to liquid rocket engine injectors using the gas/liquid shear-coaxial element in which the inner liquid cylindrical post is submerged slightly with respect to the overall exit plane of the device. Because most of the previous works focus on spray structure outside of the injector, this study provides readers with insight into unsteadiness resulting from hydrodynamic instabilities within the internal nozzle flow upstream of the combustion chamber. The present study focuses on unsteady "self-oscillations," which have been theorized by various researchers. The Kelvin–Helmholtz instability mechanism as a result of velocity discontinuity between gas and liquid phase is investigated as a source of unsteadiness that could contribute to combustion roughness or instabilities. For existing liquid-rocket-engine injectors, mass-flow variations of the order of 30–40% are shown to exist as a result of this highly nonlinear process. Fundamental frequencies are also identified for a range of conditions.

Nomenclature

CP_i	=	computational processor
D	=	channel width
f	=	nondimensional frequency
L	=	channel length
$\dot{m}$	=	total mass-flow rate throughout the injector orifice exit
P	=	pressure
Re	=	Reynolds number
t_{LOX}	=	liquid post thickness
u, v	=	velocity
V	=	computational cell volume
W_e	=	Weber number
x	=	Cartesian coordinate, x(radial) direction
y	=	Cartesian coordinate, y(radial) direction
z	=	Cartesian coordinate, z(axis) direction
α	=	void fraction
ΔU	=	velocity difference between liquid and gas phase
ϵ	=	density ratio (ρ_g / ρ_l)
μ	=	viscosity
ρ	=	fluid pseudodensity

Subscripts

g	=	gas phase
i	=	inlet
l	=	liquid phase
o	=	outlet

Introduction

COAXIAL injectors have been widely used in the liquid rocket engines, particularly those using the liquid-oxygen/hydrogen propellant combination. The concentric-orifice coaxial injector was used in rocket engine testing as early as the 1940s and later became the preferred design on most of cryogenic propellant applica-tions. Typically, liquid oxidizer is fed through the central tube, and the gaseous hydrogen/combustion products are injected around the outer annulus. Often times, the liquid-oxygen (LOX) poststructure is recessed from the injector face in order to improve the com-bustion stability. Inner liquid turbulence and gas/liquid interactions cause the liquid to be stripped away from the jet and entrained into the surrounding gasflow. Disturbances from inside the combustion chamber or outside vibrations during engine operations, along with the intrinsic jet instability inside the nozzle, create a certain circum-stance that the liquid jet cannot maintain a uniform distribution of atomized spray. Under these conditions, the injector element can produce periodic fluctuations in the combustion zone, which might or might not couple to the dynamics within the combustion chamber.

For conditions typical of liquid rocket injectors, the principal source introducing instability to the jet is the aerodynamic force generated at the gas/liquid interface as a result of the large disparity in velocities of these two streams. Reynolds and Weber numbers are generally very high in these atomizers, and aerodynamic forces are several orders of magnitude larger than capillary forces. The velocity difference between the two streams gives rise to the classic Kelvin–Helmholtz instability.

The historical review of the development of various coaxial injec-tors used in liquid engines can be found in Refs. 1 and 2. Theoretical and numerical modeling efforts on the coaxial injector atomization is also summarized in the paper of Vingert et al.[3] along with exper-imental results. Their work mainly devoted to the drop size predic-tion by using those experimental data. In the paper of Hulka and Hutt,[1] the review focused on instability phenomena associated with the combustion feed system. Series of injector testing revealed that injection velocity ratio, pressure drop after the injection, and fuel-injection temperature are the key parameters defining combustion instability.

According to the Ref. 2, a combustion instability with a high frequency is categorized as an acoustic or a hybrid instability. The acoustic instability shows a wave-type oscillation in the main cham-ber, but is independent of the feed system. In the hybrid form of insta-bility, the wave character of the oscillation is dominant as a result of a strong coupling between the feed system and the combustion cham-ber. Hutt and Rocker[4] also investigated the high-frequency combus-tion instability associated with coaxial injectors. They classified the instability phenomena in the chamber in terms of injection-coupled and intrinsic mechanisms. The injection coupling requires chamber pressure/temperature variation as a key contributor in affecting flow dynamics through the injector. The intrinsic mechanism occurs in the flowfield as a result of its own flow dynamics with negligible feed system effects.

*Graduate Research Assistant, School of Aeronautics and Astronautics; currently Research Programmer, National Center for Supercomputing Ap-plications, University of Illinois at Urbana–Champaign, IL 61820.
†Professor, School of Aeronautics and Astronautics.
‡Associate Professor, School of Aeronautics and Astronautics.

Mayer and his research group have contributed a significant amount of work on the coaxial injector in terms of the combustion instability. Mayer and Krulle[5] investigated coaxial flow mixing phenomena in terms of chamber pressure variation, density/velocity ratio changes, and surface tension effects. Increasing chamber pressure leads to proportional increases in gas density, which tend to magnify aerodynamic interaction between liquid and gas phases thereby causing faster, finer atomization. Increasing surrounding gas velocity also leads to an increase of surface wave growth and to macroscopic instabilities of the liquid jet. They claimed the initiation of the jet surface deformation was caused by internal liquid turbulence delivering energy from eddy structures of size 10–30% of the inner cylinder (a.k.a. LOX post) diameter. Their global spray simulation combining primary and secondary jet breakup showed qualitative agreement with their experimental results.

In other works of Mayer and Tamura[6] and Mayer et al.,[7] the coaxial injector flow was studied under hotfire conditions at supercritical chamber pressure (higher than 5 MPa). The study revealed a remarkable difference between subcritical spray formation and the supercrit-ical injection and mixing. At subcritical conditions, the liquid jet shows similar flow pattern to the cold-flow test forming ligaments off the liquid jet surface and producing droplets before evaporation. At supercritical conditions, droplets no longer exist, and the liquid jet rapidly dissolves. The flame from combustion chamber was anchored at the tip of LOX post by flow recirculation eddies serving as flame holder for steady-state combustion. The asymmetric flow oscillation was also reported in all experiments, but the source of the oscillation was not clearly stated.

Numerous researchers have studied wave-type, asymmetric jet oscillations in coaxial elements from both theoretical and experimental views. Eroglu and Chigier[8] focused on the wave characteristics of liquid jet from coaxial air-blast injector. They measured frequency and wavelength of the jet issuing from the injector, and found two dominant wave types: spanwise (dilational) and streamwise (sinuous) waves. The spanwise wave was prevalent at low gas/liquid relative velocities, whereas the streamwise wave was more prominent at higher gas/liquid relative velocities more applicable to conditions in liquid-rocket injectors. Average wavelengths decreased with liquid and gas velocity. The frequency band of the jet oscillation increased with the liquid jet velocity. Mansour and Chigier[9] also conducted similar research on liquid sheet instability using a two-dimensional air-assisted nozzle. The results showed the same trends as the Eroglu and Chigier's study. However, Mansour and Chigier's study probed higher velocity cases and confirmed that the frequency of the liquid sheet oscillation increased with coflowing gas velocity.

Instability mechanisms in liquid-rocket coaxial injectors were investigated experimentally by Kaltz et al.,[10] Glogowski et al.,[11] and Glogowski and Micci[12] under noncombusting conditions. Their studies showed that for the coaxial injector with the LOX post recessed into the fuel annulus the injector transitioned into a condition of resonance characterized by a whistling noise and significant modification to the overall structure of the spray caused by the strong acoustic coupling between injector hydrodynamics and spray formation. Without the recessed region, the injector operation produced a near resonance condition with a lower-amplitude whistling noise but did not make considerable changes in the spray structure. The recirculating flow near the recessed LOX post exit was also confirmed in the study, but resolution was insufficient to obtain data on frequency response of the recirculation zone.

Bazarov et al.[13–15] investigated coaxial injector flow dynamics in engine operating conditions. He identified "self-oscillation" and "self-pulsation" modes of liquid jet characteristics and suggested them as sources of high-amplitude noise during combustion, leading to combustion inefficiency. An injector element operates in strong feedback loops between chamber response and injection feed system. He claimed that high-frequency instability occurred because of the intrinsic unsteadiness of flowfield and in-teractions of the liquid jet atomization process with the combustion chamber and feed system dynamics.

Most of the previous research works summarized here have focused on flow phenomena outside of the recessed region of the injector, and the authors are aware of no prior numerical simulations within this region. Because the upstream flow in an injector provides the initial condition for the entire jet atomization process and combustion chamber acoustic characteristics along with the boundary conditions on the chamber, research work on this area is highly desirable. Motivated by Bazarov's research, a two-dimensional model was developed to investigate hydrodynamic instabilities of a liquid sheet in a recessed region.[16–18] Parametric studies were undertaken to assess the influence of gas/liquid velocity and density ratios, recess length, and the LOX post thickness. The results showed that increasing either density or velocity ratio produced higher oscillation frequency, and increasing the recess length also increased the natural frequency of the liquid sheet oscillation, leading to sheet breakup within the recessed region in some cases. These results showed the same tendency that was predicted by linear theory analysis. A recent experimental study of Branam[19] also showed results in agreement with these trends.

Based on the two-dimensional results, a three-dimensional model has been developed, and a series of simulations has been conducted using space shuttle main engine's (SSME) injector geometry and its flow properties as test cases. The model is described in the following section, and results are summarized in the subsequent portion of the paper.

Modeling Description

Numerics

A fully unsteady, three-dimensional, two-phase model has been developed utilizing a finite volume implementation of the marker and cell discretization method. The current model is based on the locally homogeneous flow (LHF) assumption in which the two phase are assumed to be in dynamic and thermodynamic equilibrium, that is, at each local point in the flow they have the same velocity and temperature and are in phase equilibrium. One should note that the LHF condition can limit the applicable case of jet consisting of infinitely small droplets. Because the droplets of the liquid jet in this case quickly assume local liquid velocity and temperature, the LHF model is successful in this study. An additional constitutive relation for the density field has been implemented in order to provide a mechanism of solving the two-phase flow with a single set of Navier–Stokes equations. This fictious "pseudo" density varies in amplitude between the liquid and gas extreme. The LHF assumption and the pseudodensity implementation allow the current model to handle the two-phase flowfield with one governing equations set rather than to compute separate sets of governing equations for each flow phase, liquid and gas in this case.

Formulation of the three-dimensional governing equations for computation are given as follows:

$$\frac{\partial \rho}{\partial t} + \frac{\partial \rho u}{\partial x} + \frac{\partial \rho v}{\partial y} + \frac{\partial \rho w}{\partial z} = 0 \tag{1}$$

$$\frac{\partial \rho u}{\partial t} + \frac{\partial \rho u^2}{\partial x} + \frac{\partial \rho u v}{\partial y} + \frac{\partial \rho u w}{\partial z} + \frac{\partial P}{\partial x}$$
$$= \frac{\partial}{\partial x} \mu \frac{\partial u}{\partial x} + \frac{\partial}{\partial y} \mu \frac{\partial u}{\partial y} + \frac{\partial}{\partial z} \mu \frac{\partial u}{\partial z} \tag{2}$$

$$\frac{\partial \rho v}{\partial t} + \frac{\partial \rho u v}{\partial x} + \frac{\partial \rho v^2}{\partial y} + \frac{\partial \rho v w}{\partial z} + \frac{\partial P}{\partial y}$$
$$= \frac{\partial}{\partial x} \mu \frac{\partial v}{\partial x} + \frac{\partial}{\partial y} \mu \frac{\partial v}{\partial y} + \frac{\partial}{\partial z} \mu \frac{\partial v}{\partial z} \tag{3}$$

$$\frac{\partial \rho w}{\partial t} + \frac{\partial \rho u w}{\partial x} + \frac{\partial \rho v w}{\partial y} + \frac{\partial \rho w^2}{\partial z} + \frac{\partial P}{\partial y}$$
$$= \frac{\partial}{\partial x} \mu \frac{\partial w}{\partial x} + \frac{\partial}{\partial y} \mu \frac{\partial w}{\partial y} + \frac{\partial}{\partial z} \mu \frac{\partial w}{\partial z} \tag{4}$$

The Lagrangian form of the continuity equation is also required:

$$\frac{D\rho}{Dt} + \rho \left(\frac{\partial u}{\partial x} + \frac{\partial v}{\partial y} + \frac{\partial w}{\partial z} \right) = 0 \tag{5}$$

Under the two-phase flow condition, the viscosity can vary spatially. According to Kubota et al.[20] viscosity of the mixture can be written as

$$\mu = \alpha \mu_g + (1 - \alpha)\mu_l \qquad (6)$$

where μ_g and μ_l are the gas and liquid viscosities. Because the nondimensional pseudodensity is the volume fraction of mass per unit cell volume, Eq. (6) can be written as

$$\mu(\rho) = \rho \mu_l + (1 - \rho)\mu_g \qquad (7)$$

This mixture viscosity is substituted back into Eqs. (2–4) for nondimensionalization. The channel width, liquid inflow velocity, and liquid density are chosen as dimensions in nondimensionalizing the equations. Then the momentum equations can be arranged as follows for the momentum flux calculation:

$$\frac{\partial \rho u}{\partial t} + \frac{\partial}{\partial x}\left(\rho u^2 - \frac{1}{Re^*}\frac{\partial u}{\partial x}\right) + \frac{\partial}{\partial y}\left(\rho u v - \frac{1}{Re^*}\frac{\partial u}{\partial y}\right)$$
$$+ \frac{\partial}{\partial z}\left(\rho u w - \frac{1}{Re^*}\frac{\partial u}{\partial z}\right) = -\frac{\partial p}{\partial x} \qquad (8)$$

$$\frac{\partial \rho v}{\partial t} + \frac{\partial}{\partial x}\left(\rho u v - \frac{1}{Re^*}\frac{\partial v}{\partial x}\right) + \frac{\partial}{\partial y}\left(\rho v^2 - \frac{1}{Re^*}\frac{\partial v}{\partial y}\right)$$
$$+ \frac{\partial}{\partial z}\left(\rho v w - \frac{1}{Re^*}\frac{\partial v}{\partial z}\right) = -\frac{\partial p}{\partial y} \qquad (9)$$

$$\frac{\partial \rho w}{\partial t} + \frac{\partial}{\partial x}\left(\rho u w - \frac{1}{Re^*}\frac{\partial w}{\partial x}\right) + \frac{\partial}{\partial y}\left(\rho v w - \frac{1}{Re^*}\frac{\partial w}{\partial y}\right)$$
$$+ \frac{\partial}{\partial z}\left(\rho w^2 - \frac{1}{Re^*}\frac{\partial w}{\partial z}\right) = -\frac{\partial p}{\partial z} \qquad (10)$$

where the Reynolds number for mixture Re^* is defined as follows:

$$1/Re^* = \rho/Re_l + [\rho_g(1 - \rho)/\rho_l](1/Re_g) \qquad (11)$$

which includes the both liquid- and gas-phase viscous effects in one term. Here Re_{e_l} and Re_{e_g} represent Reynolds numbers of liquid and gas phase, respectively.

An additional constitutive relation for the nonphysical pseudodensity variable is required in place of an equation of state in order to close the set of governing equations. Basically, the droplets in gas media are assumed to be the same size, that is, the droplet volume does not change as a result of the pressure variation of the flowfield. Neither coalescence or collision between the droplets nor the secondary breakup of droplet is considered. Consequently, one can conclude from the preceding assumptions that the density evolves in time by simply considering a Lagrangian tracking of the droplet field as specified by a continuity equation as

$$\frac{D\rho}{Dt} = \frac{\partial \rho}{\partial t} + u\frac{\partial \rho}{\partial x} + v\frac{\partial \rho}{\partial y} + w\frac{\partial \rho}{\partial z} = 0 \qquad (12)$$

This equation is basically a statement that the droplet mass is invariant along a path line in the fluid. By taking account for the flow direction, the pseudodensity is updated based on mass flux calculation as follows:

$$\rho^{n+1} = \rho^n - (\Delta t/V_c)\left[(\dot{m}_{\text{out}})_{x,y,z} - (\dot{m}_{\text{in}})_{x,y,z}\right] \qquad (13)$$

where V_c is volume of a given cell and $\dot{m}$ is mass flow rate corresponding x, y, and z directions. The flux of the mass through a given cell is calculated by a standard upwind scheme. Although this provides a locally first-order solution in the region adjacent to the discontinuity in density, it provides for a stable approach to account for the large density gradients near the interface. Because the interface region will undoubtedly contain droplets in these very high convective environments, a shock-type density discontinuity would not be consistent with a homogeneous flow representation. The scheme is second-order accurate with the exception of the points adjacent to the interface, and convergence is verified in the next section. One can find more details on development of the numerical solver in

Bunnell's work.[21] In this study, the three-dimensional coaxial jet modeling work will be presented focusing on hydrodynamic instability of the shear coaxial injector.

Parallelization

The code was run on a Beowulf Linux cluster, which is equipped with 104 processors and a fast ethernet network. One run usually required 12 to 24 processors depending on mesh discretization. Because the cluster is dedicated to the modeling, each run makes use of nearly 100% of CPU power and network bandwidth. Even with this superb environment, one simulation that runs up to 150,000 time steps takes about three weeks.

Parallel processing using message passing interface (MPI) has been implemented in order to run the three-dimensional model in a timely manner. Even with the large number of 1.2 GHz AMD Athlon processors used in the study, running a full three-dimensional computational-fluid-dynamics model in a timely, economic manner still remains a challenge.

For the present three-dimensional atomization modeling, the computational domain is split up in axial direction for the desired number of processors n. While each processor solves a flowfield of subdivided domain, the boundary conditions of each subdomain are transferred to neighboring domains through message passing. All of the processors involved in this procedure perform the same calculation in each step by copying the original task to other processors but solving different subdomains and boundary conditions. This type of parallelism is called single-program Multiple-Data (SPMD). A typical example of using the SPMD parallel process is to solve the Poisson equation.

In the finite volume marker and cell method used in this study, the mesh discretization is such that the calculation of primitive variables P, ρ, V, and the Lagrangian derivative $D\rho/Dt$, only depend on values at neighboring nodes. Therefore, boundary values on a neighboring node must be known for the calculation of primitive variables, and the data along the boundary of a given domain must be passed to its neighbors. Physically, the problem being solved in parallel on n, processors can be viewed as n, separate flowfield problems, each being solved with a different set of boundary conditions. However, the boundary conditions for each problem are dependent on the flowfield in each subdomain. For processor CP_1 the inlet boundary condition is a constant flowfield condition, as is the exit boundary condition for the flowfield being solved by CP_{n-1}. Here, the CP_i in this section denotes the computing processor corresponding to ith subdomain to be solved. The inner domain boundary conditions are function of time at the inlet and exit surfaces of a given domain and are functions of the surrounding domain flowfield.

Another issue associated with the parallelization in this modeling is the Poisson solver for the calculation of the pressure field. The system of sparse linear equations has to be solved in such a way that the solution satisfies each process domain. The original solution algorithm in two-dimensonal simulations[16,17] relies on a successive-line-overrelaxation (SLOR) method, and the parallelized solver takes the same methodology. The SLOR technique is applied to each subdomain independently, and yet each subdomain is linked to others through the message passing. The procedure is outlined as follows referring to Fig. 1: 1) sweep the first column in each domain,
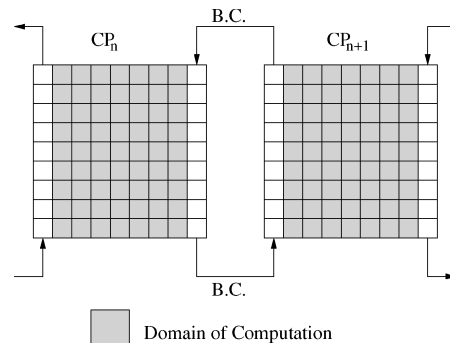

Fig. 1   Schematic of domain splitting used in parallel processing.

2) pass the result from CP_{n+1} to CP_n, 3) finish the sweep across the domain, and 4) pass the result from CP_n to CP_{n+1}.

This provides linkage of the domains at the boundaries because the SLOR sweep requires knowing the value of P at locations $i + 1$ and $i − 1$ of each domain. The communication requirements are such that two calls to MPI subroutines, MPI_SEND and MPI_RECV, must be made for each iteration. References 22–26 provide background information on MPI.

Despite the large number of processors available, speed was maximized when six grid points (minimum number of grid points decided as a result of differential schemes used in the solver) in axial direction for each individual processors were used, resulting in 12 processors of use for $72 \times 71 \times 71$ mesh. With the individual processors at this speed (1.2 GHz), the computation becomes communication limited when larger number of nodes are employed.

Grid-Refinement Tests

The computational domain consists of the LOX and gaseous hydrogen flowpath from the LOX post exit to the injector orifice exit, which is the combustion chamber face. To account for the variation in the flowfield, the domain is divided into numerous grid cells such that the volume of a computational cell is much smaller than the wavelength of the highest frequency acoustic mode to be considered.

The computational structured mesh generation consists of two parts; the inner circle for liquid phase and the outer annulus for gas-phase flow. Because of the liquid poststructure configured between the liquid cylinder and the gaseous fuel annular passage, the circular shape of physical domain has to be fixed. However, a polar coordinate mesh cannot be used because of the condition of maintaining $n \times n$ sparse matrix solver. The inner circle meshing begins with the meshing of a square. The square mesh is then deformed making use of polynomial stretching of order n in order to form a quarter of a circle. A mirror image is then symmetrically projected until it forms a complete circle. The reason that we do not extend this out to the nozzle wall is because we have to complete the circle configuration for the liquid post structure. For the outer gas-phase domain, circles surround the inner liquid part while lines in y and z directions are extended from the nodes on the outmost circle of inner domain to the injector orifice wall side. A complete cross-sectional view of a coarse computational mesh is shown in Fig. 2. Grid points in the diagonal directions create challenges because the $n \times n$ matrix size should be kept as a result of the flow solver algorithm. This problem was solved by deploying two lines in both y and z directions from the diagonal nodes to external circumference, resulting in nearly triangular-shaped cells on the diagonal directions. The liquid post tip area has the smallest grid size to resolve the recirculation zone immediately downstream of the post.

A grid-convergence test has been conducted in order to find an adequate mesh size. Three mesh sizes: $30 \times 30 \times 30$, $60 \times 60 \times 60$, and $90 \times 90 \times 90$, in x, y, and z direction, respectively, are tested, and the result is shown in Fig. 3. However, because of the run-time constraint, the test is limited to a short period of time up to 10,000 time steps. Figure 3 depicts the time history of mass flow through the injector nozzle exit for each mesh size. Although the coarse grid ($30 \times 30 \times 30$) shows unacceptable behavior with excessive diffusion, the middle size grid ($60 \times 60 \times 60$) matches fairly well with the fine grid ($90 \times 90 \times 90$). Though running with the fine grid or even finer grid would be desirable, the cost for running those fine grids requires unbearable run time (more than one month up to 10,000 time steps for $90 \times 90 \times 90$ grid size). Therefore, the middle grid size has been adopted for the three-dimensional modeling. Actual three-dimensional simulations have used a $72 \times 71 \times 71$ mesh by increasing the number of grid points by as many as possible without sacrificing a reasonable runtime.

Boundary conditions are applied to the domain as follows: along the wall of the injector, the no-slip condition is used. The liquid post tip area at the inlet plane also requires a no-slip condition. On the inflow boundary, constant liquid/gas-phase velocities are defined. The pressure is extrapolated with zero gradient for the inlet. At the exit, constant pressure is set while the velocities are extrapolated

Table 1 Schematic of SSME coaxial injector and summary of critical dimensions

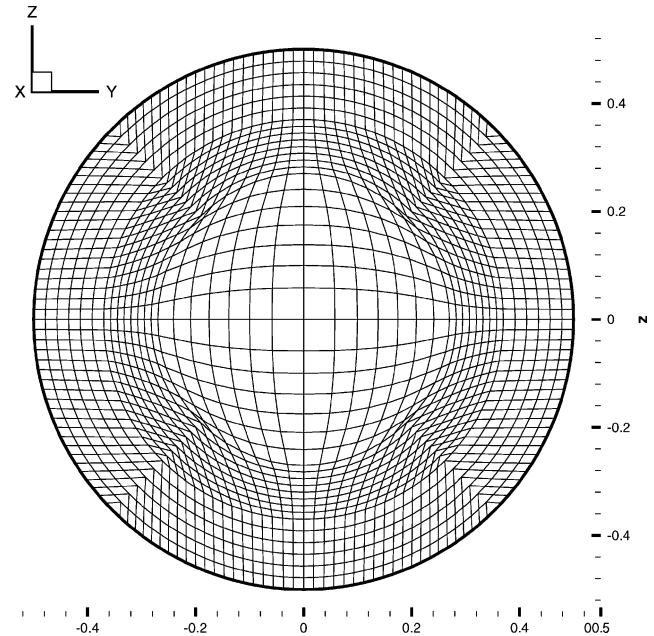| Injector geometric parameters	SSME preburner, mm	SSME mainburner, mm
Fuel annulus diameter D_f	5.03	8.84
LOX post outer diameter D_o	3.76	6.60
LOX post inner diameter D_i	2.26	4.77
Post tip thickness t_{LOX}	0.76	0.92
Recess length L	2.54	6.48

Fig. 2 Cross-sectional view of three-dimensional computational mesh: axial direction.

with zero gradient. The inflow boundary condition only holds for the initial processor used in the parallel calculation. Similarly, the exit boundary condition applies only to the last processor assigned in the parallel processing. Additional boundary conditions on both sides of each subdomain from the domain discretization are functions of time and neighboring domains.

Results

A total of five three-dimensional unsteady calculations are presented. The SSME's coaxial injector has been chosen for baseline modeling case. First, the injector of the SSME main combustion chamber (MCC) has been investigated. Further simulations have been performed for the MCC injector with a longer recess length and lower velocity ratio in order to assess the impact of these parameters. In addition, a simulation of SSME preburner injector has been conducted. Both injectors use LOX and gaseous hydrogen (GH_2) as an oxidizer and fuel respectively, but have different geometries and flow properties consistent with the fuel-rich preburner gases entering the main combustion chamber. Figure 4 and Table 1 illustrate the schematic of three-dimensional coaxial injector with geometries of main burner and preburner injectors. The physical properties of each injector flow in operating condition are provided in Table 2.

SSME Main Burner Coaxial Injector

The nondimensionalization was based on the geometries in Fig. 4, and Tables 1 and 2 by using fuel annulus diameter D_f, liquid-phase velocity U_l, and liquid density ρ_l as nondimensional parameters. Under this nondimensionalization, the LOX post inner diameter has a value of 0.55, the post tip thickness t_{LOX} is 0.05, and the recess length L is 0.75. The present result assumes a gas/liquid density ratio of 0.02 consistent with high-pressure combustion conditions. As discussed in the grid-refinement study, a mesh size of $72 \times 71 \times 71$ is used for this case. A total of 12 processors are used, and the
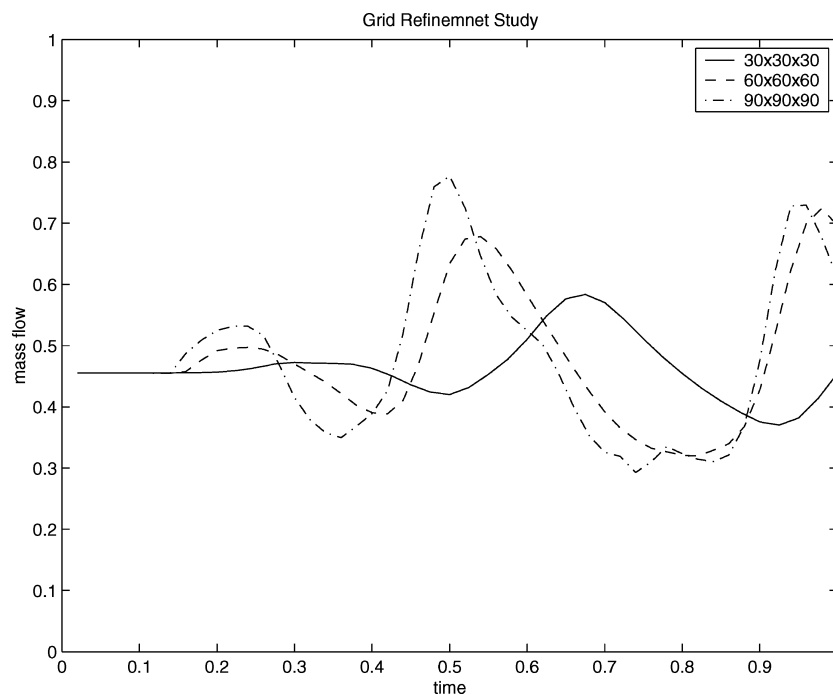
Fig. 3   Grid-refinement study on three different mesh sizes (SSME main burner condition: $\epsilon = 0.02$, $U_g/U_l = 12$, $L/D = 0.75$, $Re_l = 1.1 \times 10^6$, and $Re_g = 9.0 \times 10^5$).

Table 2   Physical properties of SSME coaxial injectors in operating conditions

Physical properties	SSME mainburner	SSME preburner
Chamber pressure, MPa	19.3	34.1
Liquid-injection velocity, m/s	31.3	30
Liquid density, kg/m³	1117	1125
Liquid Reynolds number	1.1×10^6	6.60×10^5
Gas-injection velocity, m/s	360.6	360
Gas density, kg/m³	9.47	42.5
Gas Reynolds number	9.0×10^5	3.37×10^6
Density ratio ρ_g/ρ_l	0.0085	0.038
Velocity ratio U_g/U_l	12	12
Mixture ratio liquid/gas	0.89	0.98

computational mesh is split into 12 sets, resulting $8 \times 71 \times 71$ of subdomain mesh assigned to each processor. Typically, a 150,000 time-step calculation with a time step $\Delta t = 0.0001$ (0.3 ms) takes about three weeks.

The results exhibit characteristics termed self-pulsation and self-oscillation as described by Bazarov and coworkers.[13,14] Pulsations are evident in changes in the flow rate with time, while oscillations are evidenced by azimuthal motion of the central liquid core about the annulus. Prior two-dimensional simulations[16,17] have shown similar behavior, although the azimuthal motion cannot be resolved with this decreased degree of freedom.

The overall density field behavior of the liquid jet for conditions roughly equivalent to the SSME MCC injector is illustrated in Fig. 5. Unfortunately, the model could not be run at the gas/liquid density ratio of this injector, but converged calculations were demonstrated at a density ratio approximately double that in the actual engine. Other simulations at the lower density ratio were obtained and will be discussed subsequent to this case. The left column in Fig. 5 depicts density contours in a cutaway view interpretation of the motion of the jet. The right column shows the density contours at the exit plane.

The resultant highly nonlinear, quasi-periodic oscillation occurs naturally as a result of the Kelvin–Helmholtz instability mechanism. There is no oscillation in the inflow, yet strong oscillations/pulsations develop as a result of the large relative dynamic pressure between the gas and liquid streams. The development of self-pulsation modes of the liquid jet is apparent in those figures.
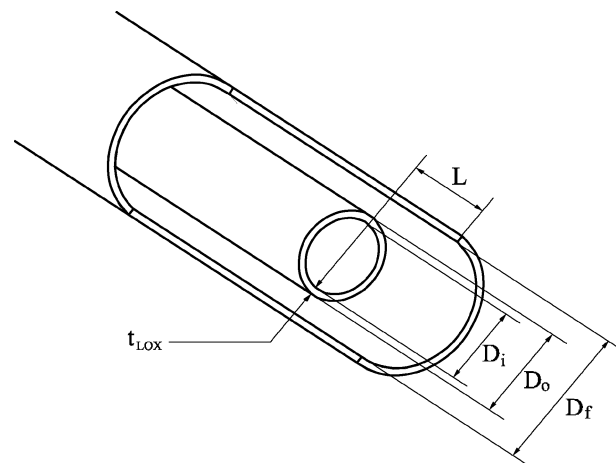

Fig. 4   Schematic of SSME coaxial injector and summary of critical dimensions.

Pressure contour plots at times corresponding to those in the density plots are shown in Fig. 6. Initially, we start the calculations assuming uniform pressure in the recessed region assessed in the computations as shown in the $t = 0$ contour. Nonlinear wave growth occurs quite rapidly, and a highly three-dimensional field develops after an initial transient period. High-pressure regions develop in accordance with azimuthal and axial motions of the structures on the jet. Longitudinal wave motion is apparent in the low pressures at times $t = 8.15$, 8.75 vs the high pressure at $t = 8.45$. Multiple high-pressure regions can be formed at different azimuthal locations within the gas annulus as evidenced in the $t = 8.90$ and 14.60 images.

Velocity streamlines of the jet in $x - y$, $x - z$, and $y - z$ planes are shown in Fig. 7 along with the velocity contours at the exit plane corresponding to the last three time frames in the density plot. The asymmetric recirculation zone in the region just downstream of the LOX post is shown in left and middle columns of the figure. The far-right column illustrates axial-velocity contours at the exit plane. Although vortices shed from the separated flow region at the base of the LOX post are evident, the velocity contours show that the jet comes out of the orifice exit at an average velocity across the entire exit plane except near the wall and flow recirculation area.
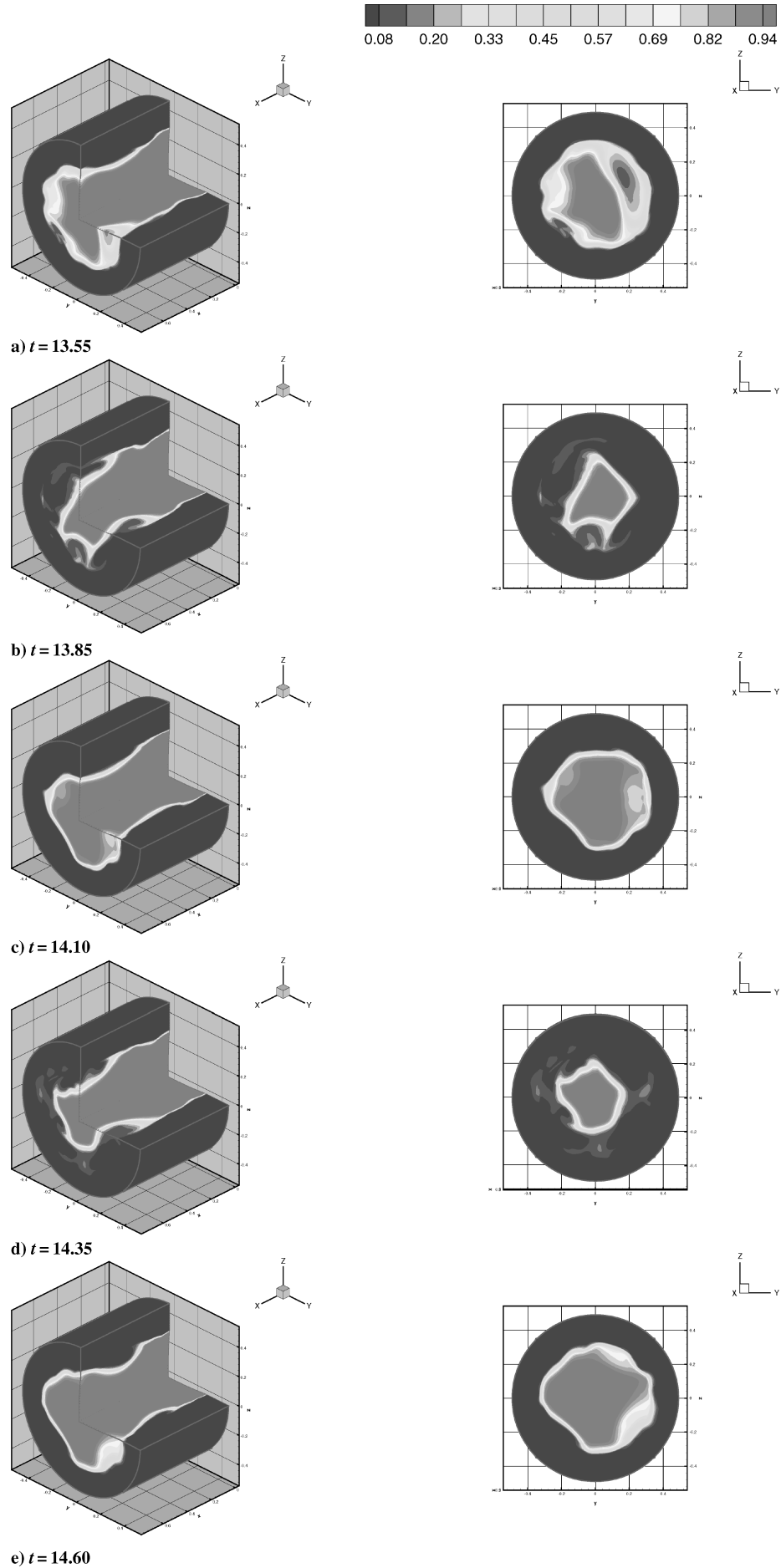
Fig. 5 Cutaway view (left column) and orifice exit plane (right column) of density contours showing typical self-pulsation: SSME main burner injector ($\epsilon = 0.02$, $U_g/U_l = 12$, $L/D = 0.75$, $Re_l = 1.1 \times 10^6$, and $Re_g = 9.0 \times 10^5$).
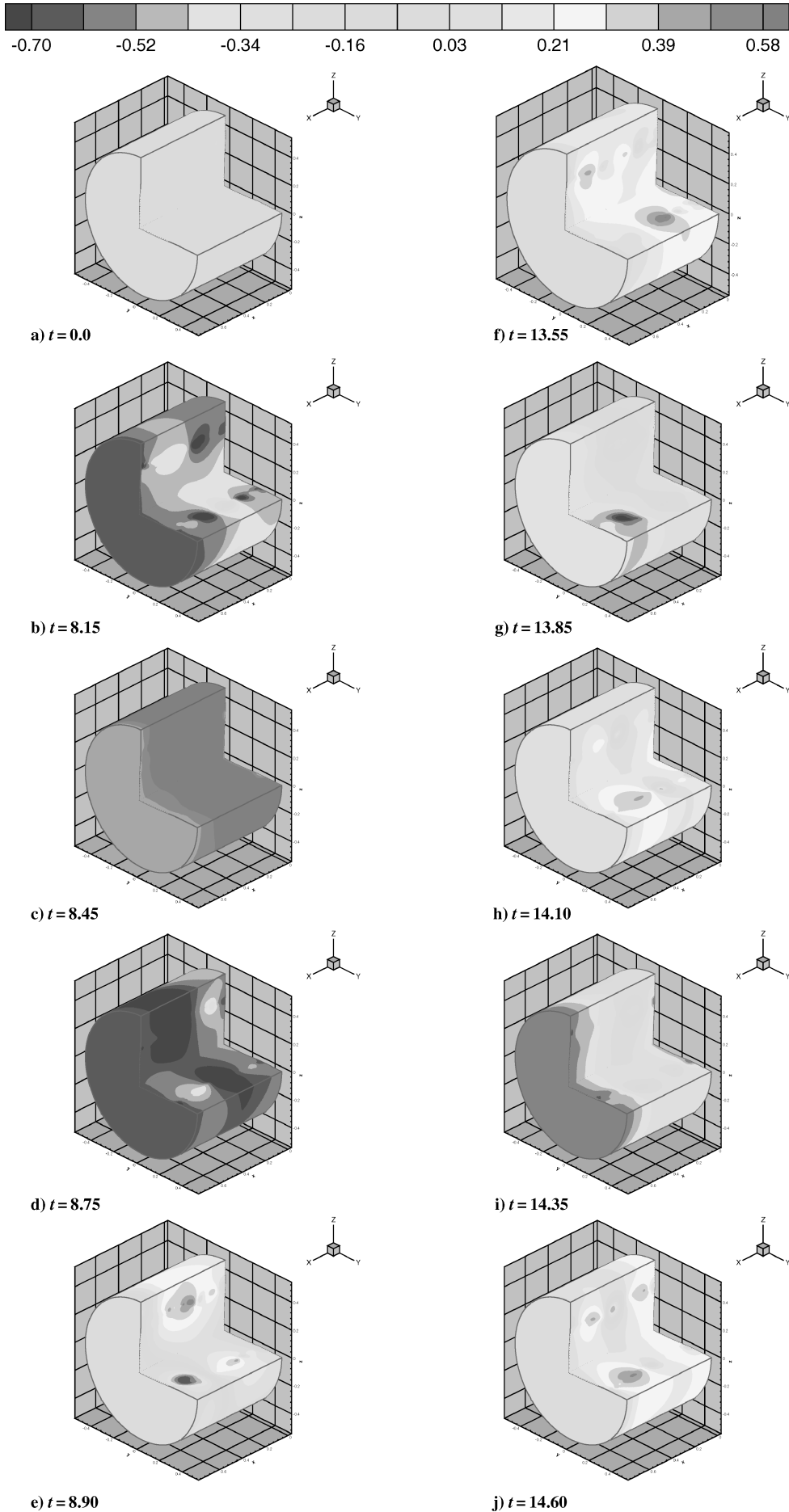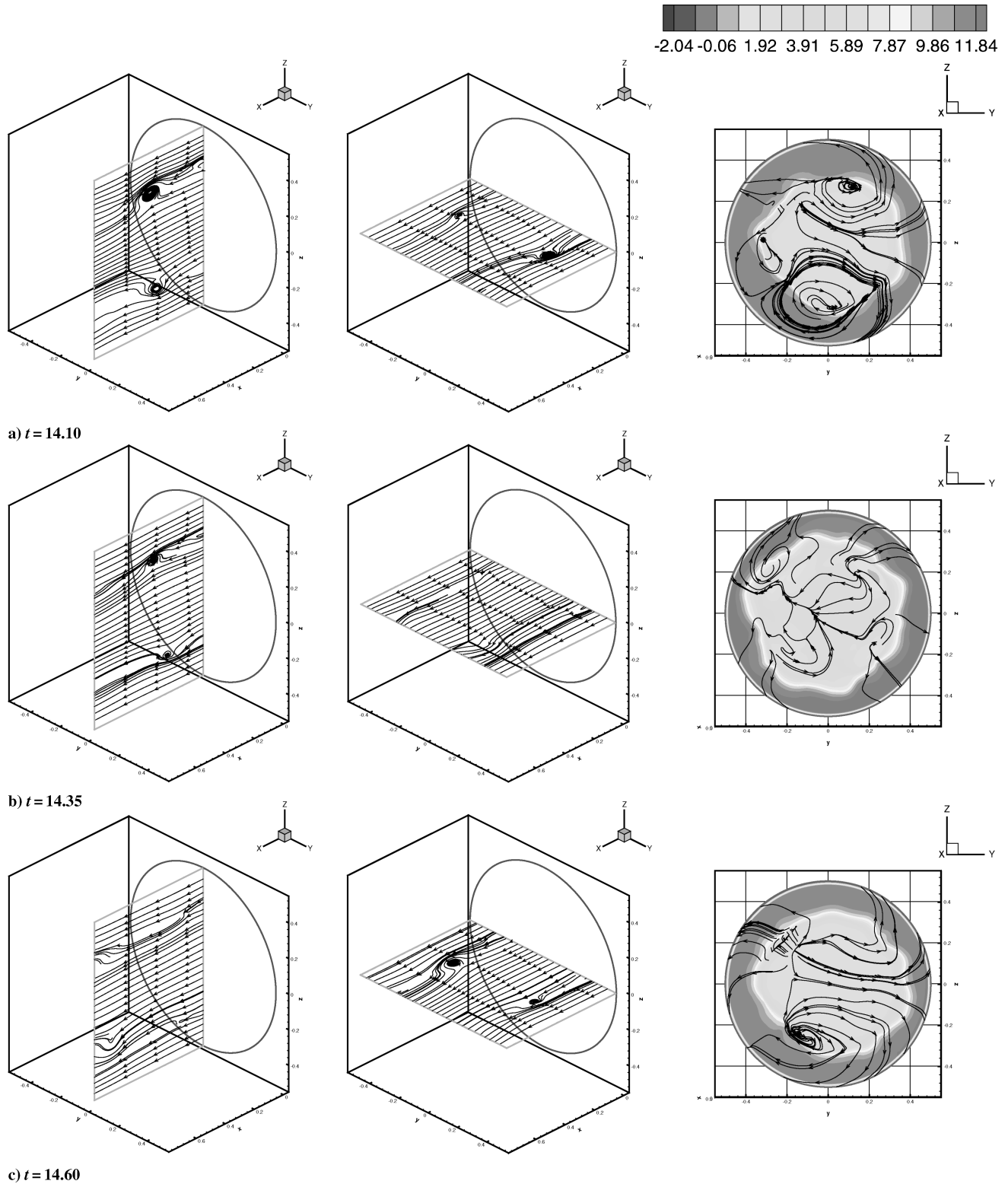
-0.70   -0.52   -0.34   -0.16   0.03   0.21   0.39   0.58

a) $t = 0.0$

b) $t = 8.15$

c) $t = 8.45$

d) $t = 8.75$

e) $t = 8.90$

f) $t = 13.55$

g) $t = 13.85$

h) $t = 14.10$

i) $t = 14.35$

j) $t = 14.60$

Fig. 6   Cutaway view (left column) and orifice exit plane (right column) of pressure contours in three-dimensional cylinder at various times: SSME main burner injector ($\epsilon = 0.02$, $U_g/U_l = 12$, $L/D = 0.75$, $Re_l = 1.1 \times 10^6$, and $Re_g = 9.0 \times 10^5$).

Fig. 7   Velocity streamlines in cross-sectional view (left and middle columns) and orifice exit plane (right column): SSME main burner injector ($\epsilon = 0.02$, $U_g/U_l = 12$, $L/D = 0.75$, $Re_l = 1.1 \times 10^6$, and $Re_g = 9.0 \times 10^5$).

This agrees with the experiment of Mayer et al.[7] which verified the rapid vanishing of the velocity difference between the central liquid jet and annular gaseous jet in the area downstream of LOX post tip. In the right column of the figure, streamlines at the orifice exit plane are depicted to indicate the complex cross currents, which develop in the channel.

One interesting bulk measure of orifice performance is the mass flow delivered at the orifice exit plane as a function of time. This quantity can be computed by quadrature of the density-axial velocity product over the exit plane area. Figure 8 shows the time history of

mass flow for the density field computed in Fig. 5 and the attendant velocity field. The unsteadiness (self-pulsations) of the jet is quite evident in this figure; mass-flow variations of 39% about the mean flow are apparent.

Spectral analysis of the data is performed in a manner commonly used for experimental data. Because the flowfield was recorded only for every hundredth time step, aliasing is expected to be a problem. That is, just as in experiments, there is reason to believe that physical processes are happening at frequencies in excess of the Nyquist frequency for the data stream. Thus, an anti-aliasing filter
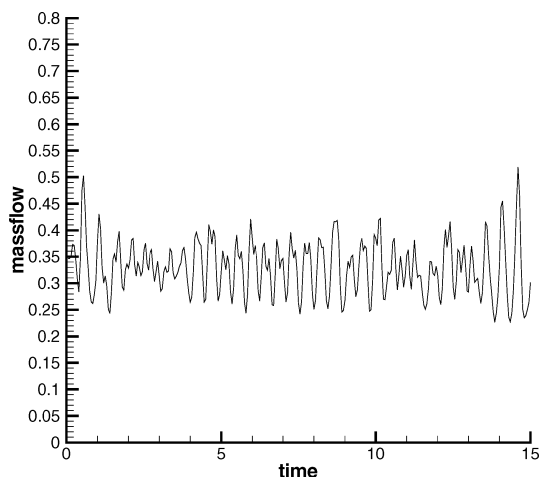
Fig. 8 Time history of mass flow at exit plane: SSME main burner injector ($\epsilon = 0.02$, $U_g/U_l = 12$, $L/D = 0.75$, $Re_l = 1.1 \times 10^6$, and $Re_g = 9.0 \times 10^5$).
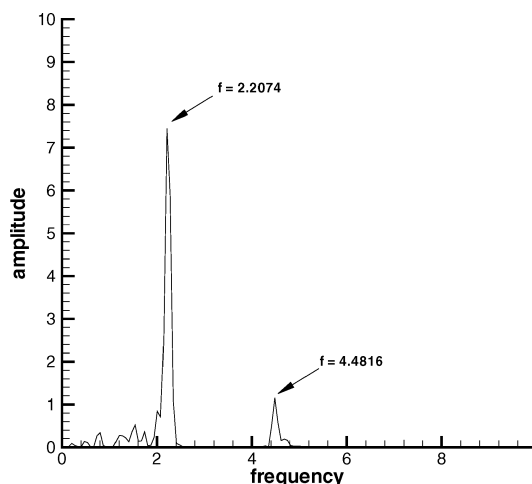

Fig. 9 Spectral analysis of mass-flow fluctuation: SSME main burner injector ($\epsilon = 0.02$, $U_g/U_l = 12$, $L/D = 0.75$, $Re_l = 1.1 \times 10^6$, and $Re_g = 9.0 \times 10^5$).

was convolved with the signal, the signal was windowed, the mean subtracted out, and the power spectrum was computed through use of a fast Fourier transform. Spectra computed without this method showed significantly worse signal-to-noise ratio when compared with those presented here.

In Fig. 9 there is a significant energy content over a range of dimensionless frequencies with a maximum at $f = 2.2074$, which represent around 7400 Hz in dimensional units. This frequency is about twice the frequency at which liquid is replaced in the submergence region. Along with the primary frequency at $f = 2.2074$, the first harmonic frequency at $f = 4.4816$ is also shown in this figure. This higher frequency corresponds to the small peak variation at the top of the primary mass flow fluctuation signal in Fig. 8, which is caused by small surface vortices coming out of the nozzle exit in an irregular manner.

In a recent study of Smith et al.,[27] the liquid core jet oscillation in a coaxial injector at supercritical condition was observed, and the frequency of flame flickering in a combustion chamber was reported as near 7000 Hz, which falls within the same frequency band of the SSME main burner coaxial injector's case. The same velocity and density ratios were used with similar geometry. Even though their coaxial injector was not exactly the same one used in this study, their experimental study provides some evidence that the liquid jet oscillation/pulsation plays a significant role in combustion response within the chamber. This is an important finding requiring further experimental verification.
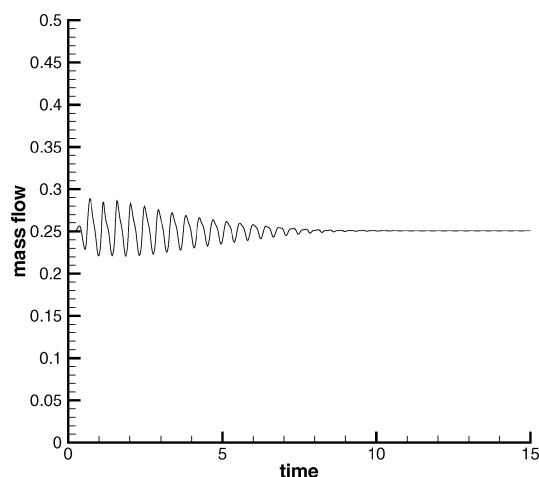

Fig. 10 Time history of mass flow at exit plane: lower velocity ratio ($\epsilon = 0.01$, $U_g/U_l = 6$, $L/D = 0.75$, $Re_l = 1.1 \times 10^6$, and $Re_g = 4.5 \times 10^5$).
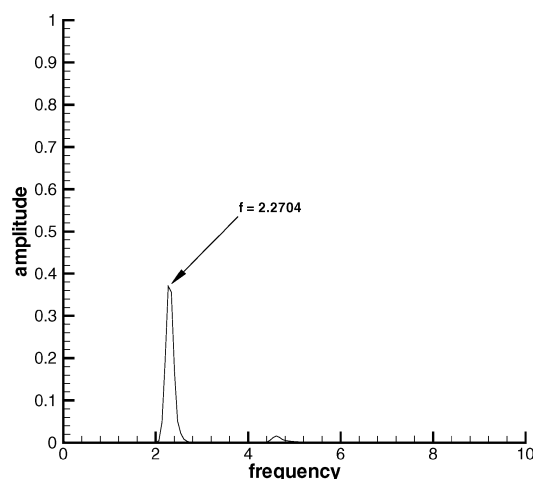

Fig. 11 Spectral analysis of mass-flow fluctuation: lower velocity ratio ($\epsilon = 0.01$, $U_g/U_l = 6$, $L/D = 0.75$, $Re_l = 1.1 \times 10^6$, and $Re_g = 4.5 \times 10^5$).

SSME MMC Injector: Lower Velocity Ratio

A case of lower velocity ratio $U_g/U_l = 6$ has been investigated in order to assess the influence of the parameter. As the gas-phase velocity is reduced to 180 m/s, the corresponding Reynolds number of the gas phase is 4.5×10^5, but the density ratio of default value (0.01) for SSME's MCC was used for this simulation. The time history of mass flow is plotted in Fig. 10. A small magnitude self-pulsation appears during the initial time period, but it decays gradually without showing any surface vortices or wave-type instability. The spectral content of the damping fluctuation signal is depicted in Fig. 11. A primary frequency at $f = 2.2704$ with very small amplitude is observed in this case; a value similar to that computed for the baseline case.

In prior two-dimensional simulations,[16,17] reductions in the relative gas/liquid velocity also showed a stabilizing influence because the dynamic pressure forcing the instability scales with the square of this velocity. However, the conclusion that the $U_g/U_l = 6$ case is stable for this injector is somewhat tenuous as our present simulation assumes a completely steady flow entering both streams. A more comprehensive analysis or confirmation via experimental data would be required to confirm the relative stability of this (or any) case.

SSME MCC Injector: Longer Recess Length

The recess length (depth) is an important parameter governing the flow process, and so a calculation was performed to assess the impact of lengthening the recess by 50% ($L = 1.25$) keeping all other parameters fixed as in the baseline MCC calculation described earlier.
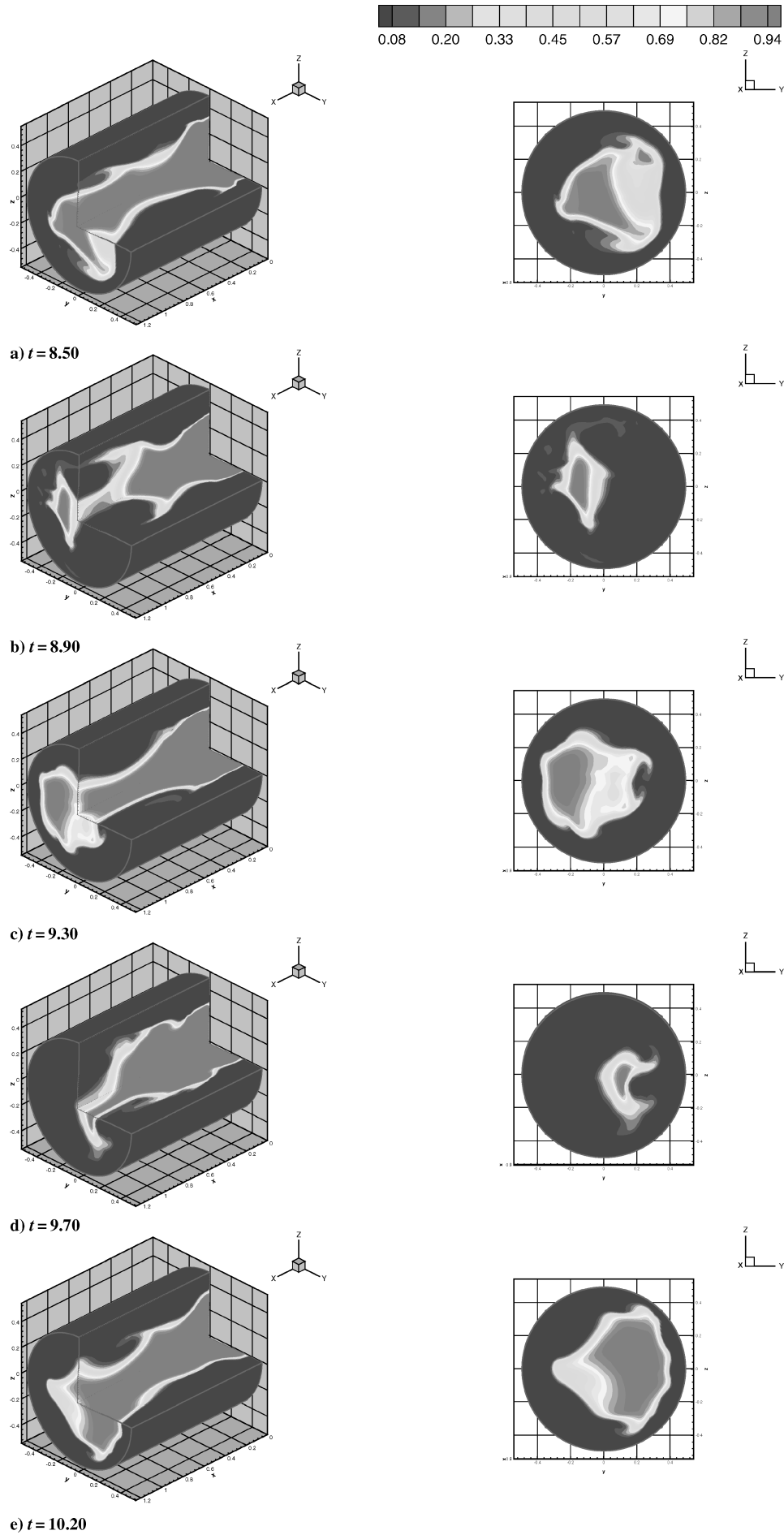
Fig. 12   Density field evolution for injector with a longer recess length: $\epsilon = 0.01$, $U_g/U_l = 12$, $L/D = 1.25$, $Re_l = 1.1 \times 10^6$, and $Re_g = 9.0 \times 10^5$.

a) $t = 9.30$

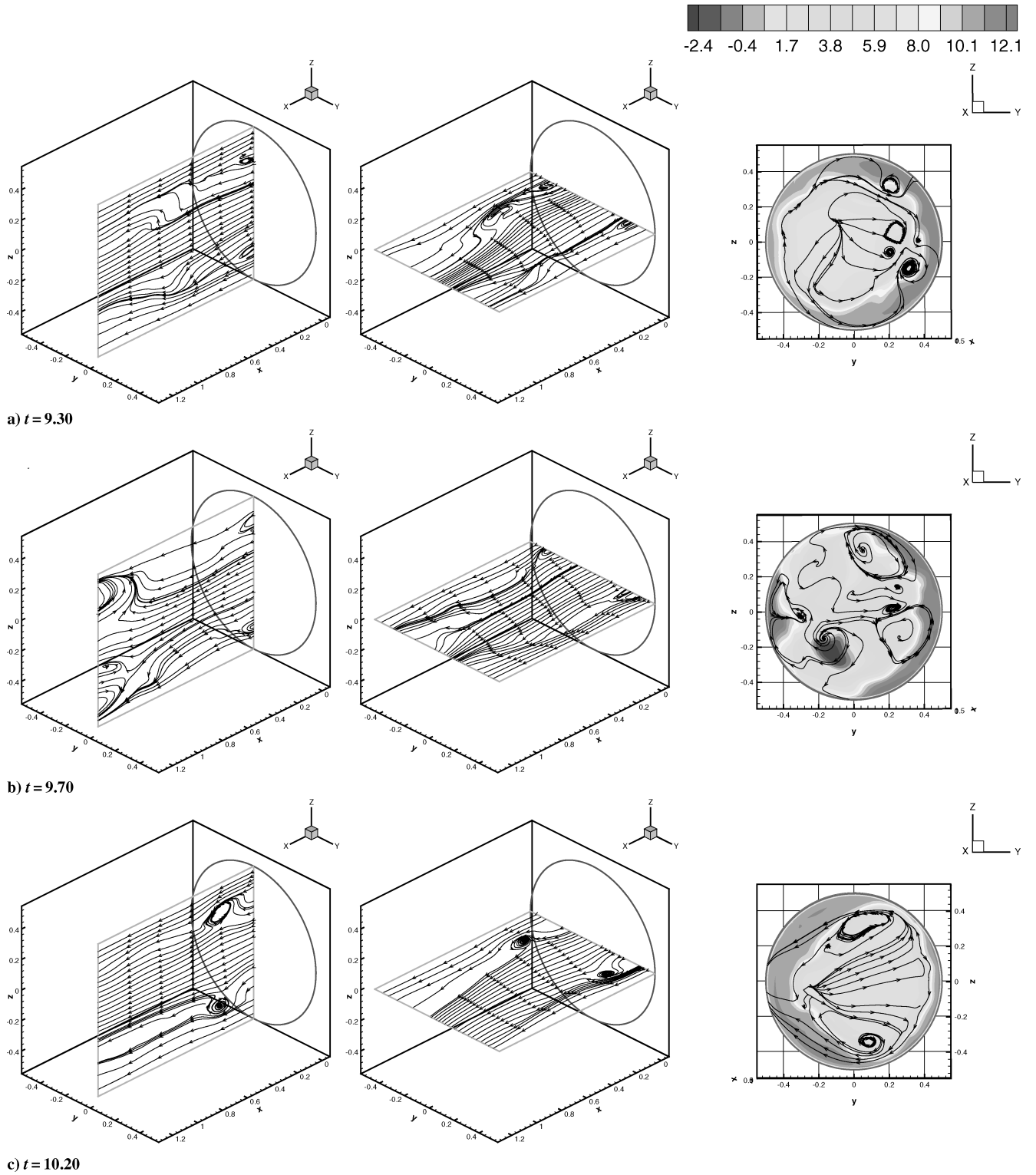**b) $t = 9.70$**

c) $t = 10.20$

Fig. 13   Velocity streamlines and contours with a longer recess length: $\epsilon = 0.01$, $U_g/U_l = 12$, $L/D = 1.25$, $Re_l = 1.1 \times 10^6$, and $Re_g = 9.0 \times 10^5$.

To keep the same grid aspect ratio and to stay within a reasonable run time, a mesh of $132 \times 75 \times 75$ is used with 22 processors. With the increased number of processors, each processor handles the same mesh size of subdomain ($8 \times 75 \times 75$) as set in the baseline case. This methodology provided an acceptable run time of about three weeks.

Density contours in three-dimensional cylinder and at the exit plane are depicted in Fig. 12. The development of self-pulsations is very clear from the beginning, and it continues to be strong through the entire modeling. Azimuthal oscillations become apparent in the latter part of the simulation as shown in the exit-plane density con-

tours in the left column. Compared to the baseline case, the liquid core moves more actively in an irregular pattern. In this simulation, the liquid jet shows a more structured wave-type motion in the axial direction. The additional flowpath length permits the longer wave instability to become more pronounced; the internal liquid jet is even seen to break up within the submerged region as shown in image (b) in the left-hand column of the figure.

The last three time frames in density contour plots are used to show velocity streamlines and axial-velocity contours at the orifice exit plane in Fig. 13. Flow recirculation is visible in the $x - y$ and $x - z$ plane in the first and second columns while velocity contours
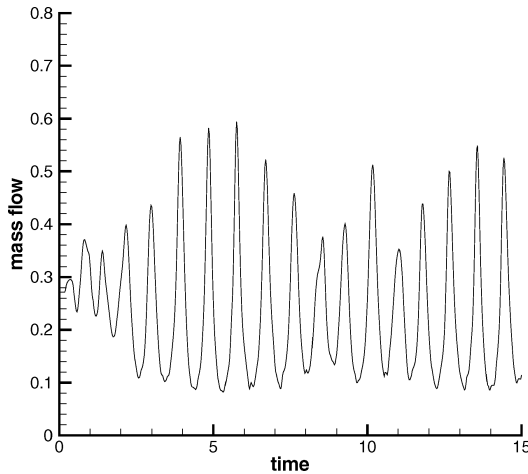
Fig. 14 Time history of mass flow at exit plane: longer recess length ($\epsilon = 0.01$, $U_g/U_l = 12$, $L/D = 1.25$, $Re_l = 1.1 \times 10^6$, and $Re_g = 9.0 \times 10^5$).
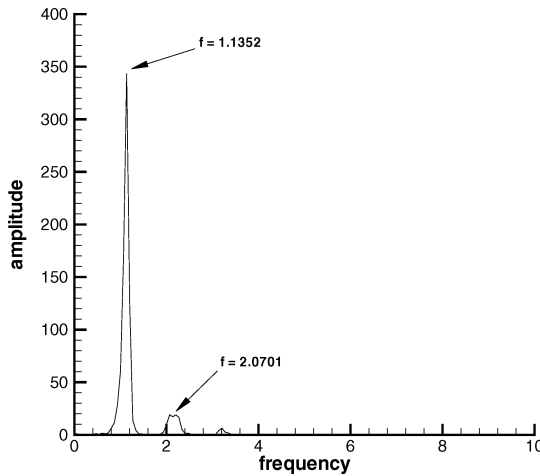

Fig. 15 Spectral analysis of mass-flow fluctuation: longer recess length ($\epsilon = 0.01$, $U_g/U_l = 12$, $L/D = 1.25$, $Re_l = 1.1 \times 10^6$, and $Re_g = 9.0 \times 10^5$).

at the exit plane are depicted in the third column with velocity streamlines in cross-stream directions. Vortex structures shed from the base of the LOX post are also evident in this case.

Figures 14 and 15 show the time history of mass flow and the spectral content of this signal, respectively. The frequency of oscillation is lower than that observed in the baseline geometry. The primary frequency is decreased to $f = 1.1352$, a little higher frequency than one at which the liquid traverses the submerged region. The magnitude of pulsation is larger, showing oscillating components of the order of 48% of the mean flow. The larger magnitude pulsation can be explained by the development of wave-type oscillation as a result of the longer recess length. Similar trends have been observed in prior two-dimensional simulations[16,17]; increasing submergence length increases the time available for instabilities to grow.

SSME Preburner Coaxial Injector

The SSME's preburner geometry is shown in Fig. 4 and Table 1, and the flow properties are tabulated in Table 2. The preburner injector has a shorter recess length ($L = 0.5$) and a three times thicker LOX post thickness ($t_{LOX} = 0.15$) than the main burner injector. The LOX post diameter D_i is 0.45, reducing the mixture ratio of liquid to gas phase significantly. The density ratio is much higher ($\epsilon = 0.04$) because of the higher pressures in this combustor, but the velocity ratio is identical to the SSME MCC baseline case. The same mesh size of $72 \times 71 \times 71$ is used for the preburner case, and so the axial resolution is somewhat better as a result of the reduced submergence length.

The simulation showed signs of weak pulsation/oscillation activity during the initial transient, but these oscillations were damped

and an essentially undisturbed jet issued from the orifice after the initial transient period. In prior two-dimensional simulations,[16-18] increasing gas density magnified the aerodynamic interaction, resulting in a higher frequency instability. However, thickening the LOX post and reducing the submergence length both had stabilizing influences on the instability. For those nondimensional LOX post thicknesses tested in the two-dimensional simulation, the frequencies corresponding to thicker LOX post were lower than the thinner LOX post. The behavior follows the definition of Strouhal number, which measures the ratio of the flow oscillation to the mean speed in the vortex-shedding dominant flowfield. In this case, those stabilizing effects more than offset the enhanced instability caused by the aerodynamic interaction at higher gas density. Therefore, the overall jet appears as stable in this case.

As noted earlier, the present simulations assume idealized conditions at the entry to the submerged region, and that the real device can indeed exhibit unsteadiness. More comprehensive simulations would be necessary to fully illuminate this issue.

Main Burner Injector Geometry with Preburner Flow Properties

The earlier result with the preburner injector case raises questions about the relation between flow properties and injector geometry. In question is whether or not geometric changes have stronger influences on the liquid jet instability than effects of changing flow properties or vice versa. To investigate the reciprocal effects between those parameters, a simulation has been conducted using the MCC injector geometry with the preburner flow properties. In summary, the recess length L is 0.75 with LOX post diameter $D_i = 0.55$ and thickness $t_{LOX} = 0.05$. The density ratio ϵ is 0.04, and velocity ratio stays at 12. The numbers in Table 2 are used for the Reynolds numbers for gas and liquidphase.

Figure 16 illustrates the limit-cycle behavior of the density contours in the passage. Pulsations and oscillations similar to those in the baseline MCC simulation are observed. One interesting observation from this case is that the pulsations/oscillations become weaker in magnitude after a certain transient period (Fig. 17). This behavior is evidenced in the orifice mass-flow history shown in Fig. 18. The main difference between this case and the MCC baseline case discussed in Figs. 5–9 is that the density ratio is twice as large. In comparison with the prior two-dimensional simulations,[16,17] the three-dimensional results generally show smaller magnitude oscillations. Because the two-dimensional liquid sheet cases have much higher liquid-to-gas mixture ratio, it leads to increasing momentum exchanges between liquid and gasphases, resulting higher liquid instability. For this particular case setup with MCC baseline geometry and the preburner flow properties, high magnitude of pulsation caused by increasing density ratio is evident during initial transient period, but it comes down to normal rage of magnitude as in the MCC baseline case. It shows that the injector geometry has a stronger effect on liquid jet instability than the flow property changes.

The spectral content of the waveform shown in Fig. 18 is shown in Fig. 19 and provides a partial explanation for the reduction in magnitude of the oscillation for this higher gas density case. Significant energy content is stored in a number of frequencies, that is, the oscillation is not organized at a single frequency, and so its overall amplitude is lower than the baseline MCC case. The same primary frequency that was observed in the baseline main burner case is present ($f = 2.0$), but in general the fluctuation is very irregular and unpredictable. Further parametric studies are required to illuminate this complex issue. All the five simulation cases stated in this section are summarized in Table 3.

Table 3 Summary of three-dimensional simulations results

Case	ϵ	U_g/U_l	L/D	t_{LOX}	$\Delta\dot{m}/\dot{m}$	Frequency
MCC	0.02	12	0.75	0.05	39	2.2 (7800 Hz)
MCC-U	0.01	6	0.75	0.05	Near 0	2.27 (8050 Hz)
MCC-L	0.01	12	1.25	0.05	48	1.14 (4800 Hz)
PB	0.04	12	0.5	0.15	Near 0	N/A
MCC-PB	0.04	12	0.75	0.05	24	0.5/1.4/2.0/4.7/5.1

a) $t = 0.0$

b) $t = 1.95$

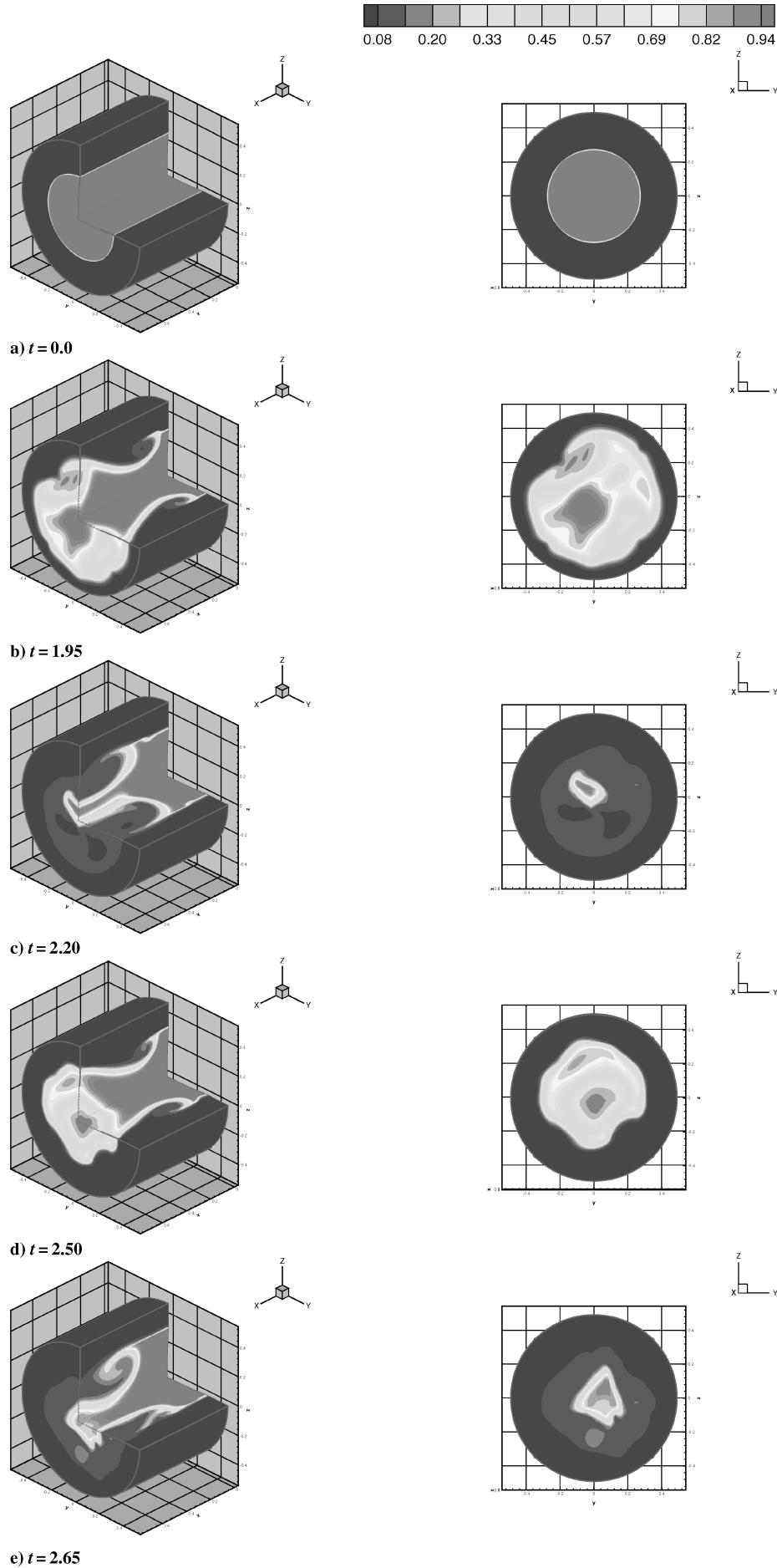c) $t = 2.20$

d) $t = 2.50$

e) $t = 2.65$

Fig. 16   Density contours in initial development of self-pulsation: $\epsilon = 0.04$, $U_g/U_l = 12$, $L/D = 0.75$, $Re_l = 6.6 \times 10^5$, $Re_g = 3.37 \times 10^6$ post thickness, and $t_{LOX} = 0.1$.

a) $t = 11.70$

b) $t = 11.90$

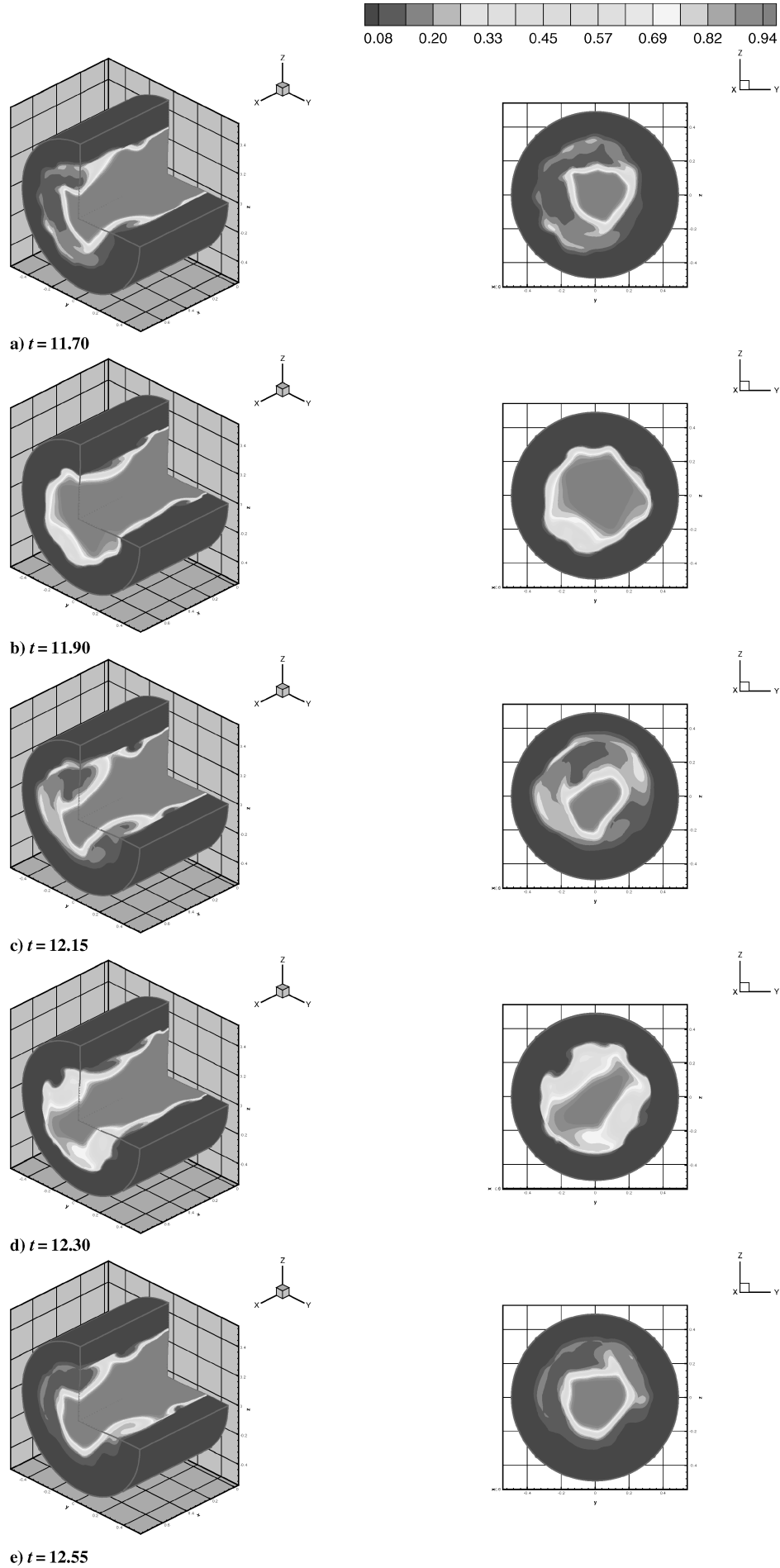c) $t = 12.15$

d) $t = 12.30$

e) $t = 12.55$

Fig. 17   Density contours in small magnitude self-pulsation mode: $\epsilon = 0.04$, $U_g/U_l = 12$, $L/D = 0.75$, $Re_l = 6.6 \times 10^5$, and $Re_g = 3.37 \times 10^6$.
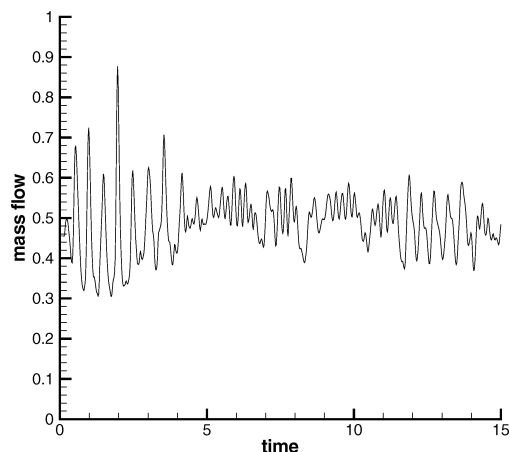
Fig. 18   Time history of mass flow at exit plane: main burner geometry with preburner flow properties ($\epsilon = 0.04$, $U_g/U_l = 12$, $L/D = 0.75$, $Re_l = 6.6 \times 10^5$, and $Re_g = 3.37 \times 10^6$).
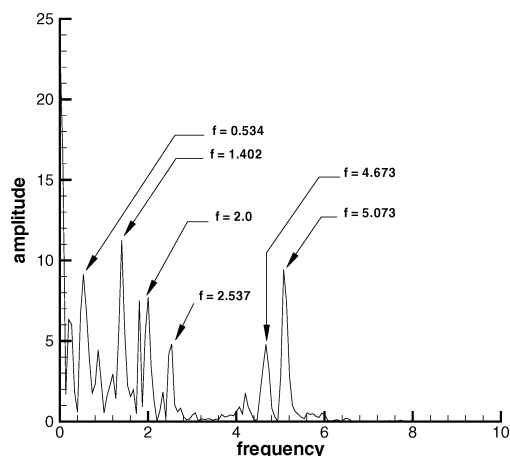

Fig. 19   Spectral analysis of mass-flow fluctuation: $\epsilon = 0.04$, $U_g/U_l = 12$, $L/D = 0.75$, $Re_l = 6.6 \times 10^5$, and $Re_g = 3.37 \times 10^6$.

Summary

A three-dimensional incompressible, unsteady, viscous Navier–Stokes solver for two-phase flow has been developed for full three-dimensional simulations of coaxial injectors in liquid rocket engines. The space shuttle main engine's (SSME) main burner and preburner injectors served as baseline modeling cases.

High-amplitude hydrodynamic instabilities are observed in the recessed region for several of the cases studied. The resulting frequencies and mass-flow variations for the five simulations are summarized in Table 3. The parameter whose effect was investigated is underlined. The mass flow of the device oscillates as much as 48% about the mean flow for the cases studied, indicating a strong presence of self-pulsations as theorized by other researchers. Oscillations of the liquid core jet about the gas annulus are also observed in some of the cases. Reduction in the length of the recess region or the velocity difference between the streams serves as a stabilizing influence. Increases of gas density introduced complex effects in terms of spectral content and amplitude of the mass-flow oscillations.

For the SSME main combustion chamber injector, the primary harmonic frequency was about 7800 Hz. Recent experiments at DLR at comparable conditions indicated flickering of the flame at a similar frequency of 7000 Hz. For this reason, there can be strong connections between hydrodynamic instabilities and the resultant combustion processes. Additional studies are recommended for complete verification of this important conclusion.

Acknowledgment

References

[1]Hulka, J., and Hutt, J. J., "Instability Phenomena in Liquid Oxygen/ Hydrogen Propellant Rocket Engines," *Liquid Rocket Engine Combustion Instability*, edited by V. Yang and W. E. Anderson, Progress in Astronautics and Aeronautics, Vol. 169, AIAA, Washington, DC, 1995, pp. 39–72.

[2]Gill, G. S., and Nurick, W. H., "Liquid Rocket Engine Injectors," NASA SP-8089, March 1976.

[3]Vingert, L., Gicquel, P., and Lourme, D., "Coaxial Injector Atomization," *Liquid Rocket Engine Combustion Instability*, edited by V. Yang and W. E. Anderson, Progress in Astronautics and Aeronautics, Vol. 169, AIAA, Washington, DC, 1995, pp. 145–190.

[4]Hutt, J. J., and Rocker, M., "High-Frequency Injector-Coupled Combustion," *Liquid Rocket Engine Combustion Instability*, edited by V. Yang and W. E. Anderson, Progress in Astronautics and Aeronautics, Vol. 169, AIAA, Washington, DC, 1995, pp. 345–356.

[5]Mayer, W., and Krulle, G., "Rocket Engine Coaxial Injector Liquid/Gas Interface Flow Phenomena," *Journal of Propulsion and Power*, Vol. 11, No. 3, 1995, pp. 513–518.

[6]Mayer, W., and Tamura, H., "Flow Visualization of Supercritical Propellant Injection in a Firing LOX/GH2 Rocket Engines," AIAA Paper 95-2433, July 1995.

[7]Mayer, W., Schik, A., and Schäffler, M., "Injection and Mixing Processing in High-Pressure Liquid Oxygen/Gaseous Hydrogen Rocket Combustors," *Journal of Propulsion and Power*, Vol. 16, No. 5, 2000, pp. 823–828.

[8]Eroglu, H., and Chigier, N., "Wave Characteristics of Liquid Jets from Airblast Coaxial Atomizers," *Atomization and Sprays*, Vol. 1, No. 4, 1991, pp. 349–366.

[9]Mansour, A., and Chigier, N., "Dynamic Behavior of Liquid Sheet," *Physics of Fluids A*, Vol. 3, No. 12, 1991, pp. 2971–2980.

[10]Kaltz, T., Milicic, M., and Glogowski, M., "Shear Coaxial Injector Spray Characterization," AIAA Paper 93-2190, June 1993.

[11]Glogowski, M., Bar-Gill, M., Puissant, C., Kaltz, T., Milicic, M., and Micci, M., "Shear Coaxial Injector Instability Mechanisms," AIAA Paper 94-2774, June 1994.

[12]Glogowski, M., and Micci, M. M., "Shear Coaxial Injector Spray Characterization near the LOX Post Tip Region," AIAA Paper 95-2552, July 1995.

[13]Bazarov, V. G., and Yang, V., "Liquid-Propellant Rocket Engine Injectors Dynamics," *Journal of Propulsion and Power*, Vol. 14, No. 5, 1998, pp. 797–806.

[14]Bazarov, V. G., and Lyul'ka, L. A., "Nonlinear Interactions in Liquid Propellant Rocket Engine Injectors," AIAA Paper 98-4039, July 1998.

[15]Bazarov, V. G., "Self-Pulsations in Coaxial Injectors with Central Swirl Stage," AIAA Paper 95-2358, July 1995.

[16]Kim, B., "Study of Hydrodynamic Instability of Shear Coaxial Injector Flow in a Recessed Region," Ph.D. Dissertation, School of Aeronautics and Astronautics, Purdue Univ., West Lafayette, IN, Dec. 2002.

[17]Kim, B., and Heister, S. D., "Two-Phase Modeling of Hydrodynamic Instabilities in Coaxial Injectors," *Journal of Propulsion and Power*, Vol. 20, No. 3, 2004, pp. 468–479.

[18]Kim, B., and Heister, S. D., "Two-Phase Modeling and Hydrodynamic Instability Study of Shear Coaxial Injector Flow," AIAA Paper 2002-3696, July 2002.

[19]Branam, R., Schneider, G., Volpp, A., and Mayer, W., "Injection Characteristics on the Surface of a Coaxial Jet," AIAA Paper 2002-3695, July 2002.

[20]Kubota, A., Kato, H., and Yamaguchi, H., "A New Modeling of Cavitating Flows: A Numerical Study of Unsteady Cavitation on a Hydrofoil Section," *Journal of Fluid Mechanics*, Vol. 240, July 1992, pp. 59–96.

[21]Bunnell, R. A., Heister, S. D., Yen, C., and Collicott, S. H., "Cavitating Injector Flows: Validation of Numerical Models and Simulations of Pressure Atomizers," *Atomization and Sprays*, Vol. 9, No. 5, 1999, pp. 445–465.

[22]Message Passing Interface Forum, "MPI: A Message-Passing Interface Standard," *International Journal of Supercomputing Applications*, Vol. 8, No. 3/4, 1994, URL: ftp://netlib2.cs.utk.edu/mpi/mpi-report.ps. available from ftp://netlib2.cs.utk.edu/mpi/mpi-report.ps.

[23]Gropp, W., and Lusk, E., "Installation Guide to mpich, a Portable Implementation of MPI," Mathematics and Computer Science Div., Argonne National Lab., Argonne, IL, ANL-96/5, 1996.

[24]Gropp, W., and Lusk, E., "User's Guide for mpich, a Portable Implementation of MPI," Mathematics and Computer Science Div., Argonne National Lab., Argonne, IL, ANL-96/6, 1996.

[25]PACS Training Group, "Introduction to MPI," National Center for Supercomputing Applications (NCSA), Univ. of Illinois, http://webct.ncsa. uiuc.edu:8900/public/MP/index.html, 2000.

[26]Pacheco, P. S., *Parallel Programming with MPI*, Morgan Kaufman, San Mateo, CA, 1997.

[27]Smith, J., Klimenko, D., Claus, W., and Mayer, W., "Supercritical LOX/Hydrogen Rocket Combustion Investigations Using Optical Diagnostics," AIAA Paper 2002-4033, July 2002.